Evolution of Production and Transport Characteristics of Steeply-Dipping Ultra-Thick Coalbed Methane Reservoirs

Shun Liang [1,2], **Hao Han** [1,*] , **Derek Elsworth** [2], **Xuehai Fu** [3], **Qiangling Yao** [1] ,
Junqiang Kang [2,3], **Xin Li** [4] **and Xuehua Li** [1]

1   State Key Laboratory of Coal Resource and Mine Safety, School of Mines, China University of Mining and Technology, Xuzhou 221008, China; 5756@cumt.edu.cn (S.L.); yaoqiangling@cumt.edu.cn (Q.Y.); lixuehua@cumt.edu.cn (X.L.)
2   EMS Energy Institute, G3 Center and Energy and Mineral Engineering, Pennsylvania State University, University Park, PA 16802, USA; elsworth@psu.edu (D.E.); kshif@cumt.edu.cn (J.K.)
3   Key Laboratory of CBM Resources and Reservoir Formation Process, Ministry of Education, China University of Mining and Technology, Xuzhou 221008, China; fuxuehai@cumt.edu.cn
4   School of Geology and Mining Engineering, Xinjiang University, Urumchi 830047, China; lixinwaxj@xju.edu.cn
*   Correspondence: TS18020011A31@cumt.edu.cn; Tel.: +86-198-5162-5361

check for updates

Abstract: The large spatial variability of in-situ stress and initial reservoir pressure in steeply-dipping ultra-thick coalbed methane (UTCBM) reservoirs exert strong control on the initial distribution of stress-sensitive permeability. This results in significant differences in the propagation of reservoir depressurization, gas production characteristics, distribution of fluid saturation, and evolution of permeability relative to flat-lying and thin counterpart coalbed methane (CBM) reservoirs. We contrast these responses using the Fukang mining area of the Junggar Basin, Xinjiang, China, as a type-example using coupled hydro-mechanical modeling. Production response indicates: (1) Dual peaks in CBM production rate, due to the asynchronous changes in the gas production rate in each the upper and lower sections of the reservoir; (2) higher depressurization and water saturation levels in the lower section of the reservoir relative to the upper at any given distance from the production well that ameliorate with time to be similar to those of standard horizontal reservoirs; (3) the heterogeneity in effective stress is further amplified by the asymmetry of the initial pressure drawdown distribution of the reservoir to exert extreme control on the down-dip evolution of absolute permeability—with implications for production. Field drainage data and simulation results obtained in this study more accurately reflect the drainage characteristics of the steeply-dipping UTCBM reservoirs. For ultra-thick low-rank coal seams, permeability anisotropy plays an important role in determining the utility of horizontal wells and hydraulic fracturing to maximize rates and yields CBM production, and requiring further study.

Keywords: large dip angle; ultra-thick; coalbed methane; dual peak production; anisotropic permeability; stress heterogeneity

1. Introduction

Coalbed methane (CBM) is an important unconventional energy resource with gas stored mainly in the adsorbed state [1–3]. Effective drainage of CBM both reduces the risk in later coal mining (for example, gas explosion accidents can be reduced >70%) and also provides low-carbon, clean and efficient energy [4,5]. Total estimates of CBM resources in the world are more than 229 trillion m³,

mainly located in Russia, Canada, China, Australia, and the United States [6,7]. In China, the total CBM resource located shallower than 2000 m is 36.8 trillion m^3-ranking third in the world [8]. However, the majority of the resource is at greater burial depths, posing major challenges in the development of CBM [9,10]. To spur efficient development of CBM resources in China, it is necessary to understand the mechanism of CBM migration and the main controlling factors for these deep ultra-thick reservoirs.

The main CBM basins (and their special characteristics) in China are the Ordos (deep seams), Qinshui (high-ranking), Junggar, and the western Guizhou region (multilayer thin coal seams) basins. The CBM reservoirs in the Fukang mining area, located in the southern margin of the Xinjiang's Junggar Basin, are characterized by large dip angles (35° to 85°), very high thicknesses (38 m to 47 m), and low-rank coal. For steeply-dipping reservoirs, stress and pressure grow rapidly down-dip, especially impacting permeability distribution and evolution [11,12]. When vertical wells are adopted for production, the initial geological conditions (reservoir pressure, ground stress, and permeability) of the upper and lower sections of the reservoir are asymmetrically distributed around the drainage wells (Figure 1). This results in significant differences in the depressurization and gas production characteristics, as well as changes in the fluid saturation distributions and permeability evolution between inclined and flat coal seams. Many studies have been conducted for CBM drainage in flat and slightly inclined (≤5°) CBM reservoirs, but few for steeply-dipping reservoirs [13–16]. Buoyant rise of desorbed free gas results in strong gradients of saturation within vertical reservoirs that ultimately impacts depressurization propagation scales, velocity rates, and inter-well interference [13,14].
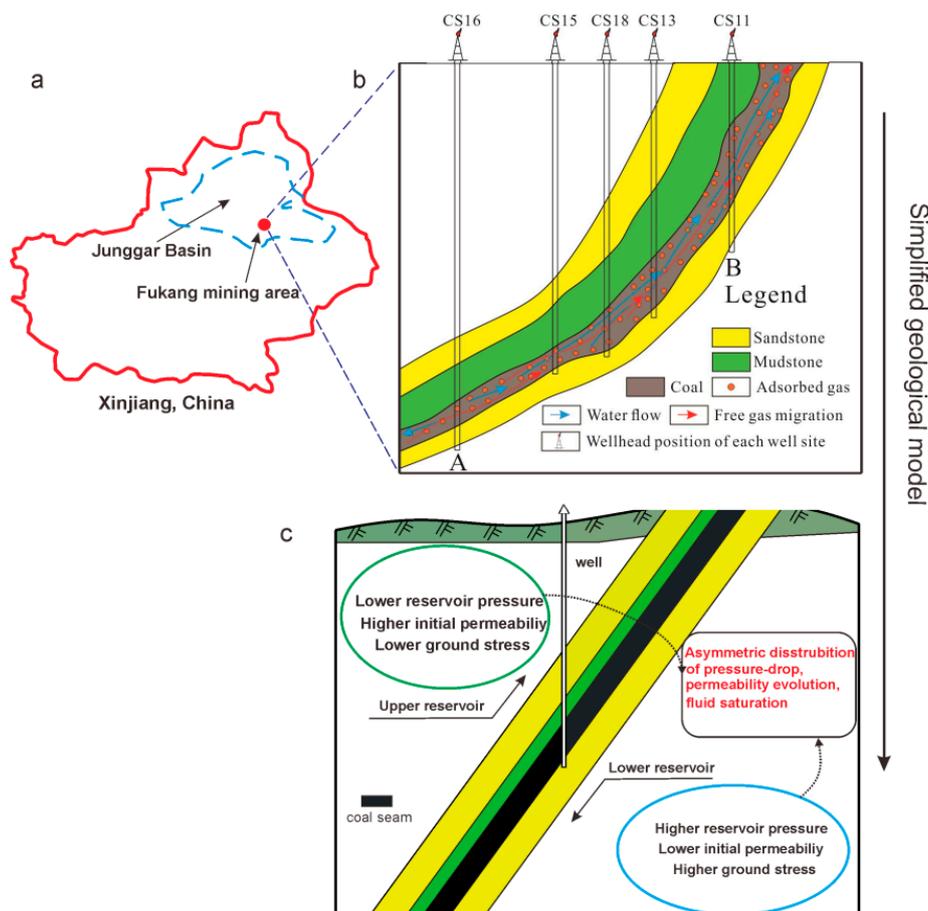

Figure 1. Characteristics of steeply-dipping coalbed methane (CBM) reservoirs, (**a**) location of the study area in China, (**b**) characteristics of the coal seams in the Badaowan Formation of the west Fukang Block [16], (**c**) a simplified geological model of a steeply-dipping CBM reservoir.

Prior studies of steeply-dipping UTCBM reservoirs ignoring stress effects have shown increased production from the shallow reservoir and the occurrence of dual peaks in maximum reservoir production, resulting from asynchronous drawdown profiles between shallow and deep [15,16]. This highlights the potential to select different well deployment selections to optimize the particular structural characteristics of these reservoirs [17]. These prior results have been primarily observational [13,14,17], and although rich in reported field observations [16] did not systematically examine the various key mechanistic controls—attempted in the following.

Coal permeability is an important parameter for CBM production and ECBM recovery [18–20]. There are generally two competing effects on the absolute permeability evolution of the coal. Firstly, depressurization increases the effective reservoir stress and causes reductions in permeability, due to cleat compression. Then, due to coal matrix shrinkage, which would moderate the cleat compression, the permeability may tend to rebound [21–24]. Moreover, CBM production usually begins with the dewatering of the coal seams for the purpose of reducing the reservoir pressure and liquid saturation [25]. Therefore, for many CBM reservoirs, the characteristics of the gas-water two-phase flow through the coal seams will play crucial roles in both water and gas production. Meanwhile, the relative permeability, which is a function of the gas or water saturation in a reservoir, will become the key parameter of the two-phase flow [26–28]. The permeability evolution of steeply-dipping reservoirs tend to differ from those of flat reservoirs during production processes as follows: (1) Due to the large dip angles of the reservoirs, the factors related to the gravity of the water, initial reservoir pressure differences, various initial permeability and in-situ stress between the deep and shallow depths, may all lead to major differences in the ranges of asymmetric depressurization and propagation velocity within the upper and lower reservoirs; (2) The asymmetric reservoir depressurization and permeability evolution may also lead to asymmetric distributions of the water saturation in the upper and lower reservoir areas, and further, affect the migration of the gas and water by controlling the relative permeability of the fluids. The development of steeply-dipping UTCBM reservoirs is considered to be multi-physics field coupling problems involving the seepage and mechanical fields. To realize theoretically the most realistic simulation results, it is important to fully consider the interaction parameters, including each of the physical fields [29].

At present, a fully coupled hydro-mechanical model has been developed to quantify the complex evolutionary processes related to gas or water transport, and coal deformation. The coupling relationships are realized through porosity and permeability models [25,27,30]. Subsequently, considering the impacts of thermal, a relatively complex coupled thermo-hydraulic-mechanical model is investigated, and the temperature, seepage, and stress fields are found to be connected by the dynamic changes in the reservoir permeability and porosity [31–33]. Recently, a more complicated model, involved thermo-hydro-mechanical-chemical responses of CO_2 enhanced CBM recovery, in which the coupling relationships of the competitive sorption between CO_2 and CH4, gas, and water two-phase transport, thermal expansions, non-isothermal gas adsorption, and coal deformations are considered [34]. The above-mentioned coupling models are able to provide some valuable references for the establishment of mathematical and physical models in this study. However, it is found that the previous research objects are generally flat reservoirs, which meant that the initial reservoir pressure, permeability, in-situ stress, and other parameters had all been fixed values. Therefore, since all of these factors are contrary to the actual characteristics of steeply-dipping reservoirs, their conclusions are deemed to be not fully applicable in this study.

We address these key issues of a lack of physically-based models of steeply-dipping UTCBM reservoirs through coupled hydro-mechanical modeling of CBM exaction. The modeling considers the key impacts of buoyant flow and differing reservoir structure and stress state in the upper and lower reservoir. We use modeling to follow depressurization, fluid saturation distributions, gas-water productivity characteristics, and permeability evolution and link this to field observations. These results are used to optimize the layout of wells for effective drainage and the future development of CBM reservoirs characterized by steep-dip angles and large thicknesses.

2. Mathematical Model

The coal seam may be typified as dual-porosity systems consisting of micro-pores in a matrix and fractures (cleats). The matrix contains adsorbed gas with the cleat system providing an effective flow path for both water and gas. CBM production begins with the dewatering of the coal seam to recover the desorbing gas. Fluid flows within the fractures satisfy Darcy's Law, and the gas diffusion between the matrix and fractures follows Fick's Law [35]. The general process of methane and water migration in the coal seam is schematically shown in Figure 2. CBM extraction also involves the complex interactions between hydrological and mechanical fields, which exert strong influences on the fluid transport processes within the coal seam. These "coupled processes" include influence effects on the gas desorption and flow processes and coal deformations, as well as porosity and permeability changes [36]. A set of field governing equations are defined that govern coal deformation, and the transport of fluids are defined that assume: (a) The coal seam is a single-permeability poroelastic continuum with dual-porosity interaction between matrix pores and fractures; (b) Water is present and migrates only in the fractures, and the methane exists and migrates in both the matrix micro-pores and fractures, with the fractures saturated by both methane and water. The adsorbed gas in the matrix, and the water in the fractures, are considered to be the principal sources of the gas and water seepage fields, respectively; (c) The methane is adsorbed on the pore surfaces of the matrix and satisfies Langmuir isothermal adsorption; (d) The fractures are saturated by both methane and water; (e) The methane is an ideal gas; (f) Buoyant transport of both water and gas are considered; (g) The coal seam is isotropic and homogeneous. The derivations of the coupled hydro-mechanical model are presented in Appendix A.
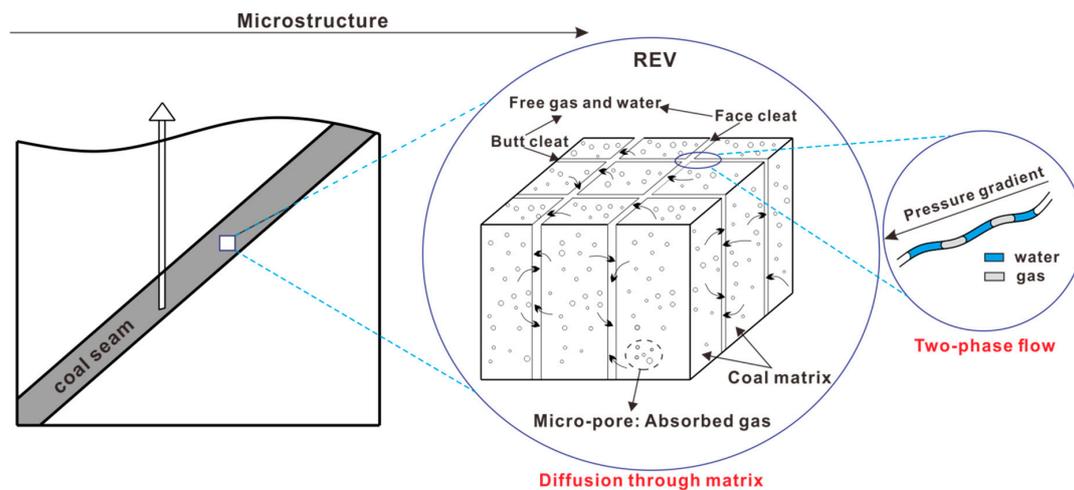

Figure 2. Methane and water migration mechanisms in a steeply-dipping coal seam.

3. Model Implementation and Analysis Results

3.1. Model Implementation

Model Implementation

This study simplifies the engineering practices of the CBM drainage in the western section of the Fukang Mining Area, located in the southern margin of the Junggar Basin, China, and a single vertical well drainage system and its mining processes are simulated. The extraction of the CBM buried at a depth of 800 m is simulated as a single vertical well. A representative physical model of a square reservoir block measuring 400 m × 600 m × 500 m is constructed. Then, by combining the actual stratum conditions in the field with the simulation data, the dip angle of the coal seam in the model is set as 45°, and the thickness of the coal is set to 20 m (Figure 3a). The buried depth of the upper part of the model is established as 1000 m, and a constant equivalent load is applied to the

upper boundary of the model according to the average volume weight of the overlying strata of the coal seam. The boundaries around and at the bottom of the model are fixed. The drainage well is located in the middle of the coal seam, with a diameter of 0.2 m. All of the external boundaries are adiabatic and non-permeable for both the CBM and water. Therefore, under the initial conditions, the coal seam is considered to be in a state of free stress, and the initial reservoir pressure is determined by the reservoir pressure gradient. To facilitate this study's quantitative analysis, a plane perpendicular to the normal direction of the coal seam is taken as the observation plane in the middle of the coal seam. Two lines (AB and CD) are set in the middle of the observation plane in Figure 3b. To quantitatively analyze the gas-water variation characteristics in the up-dip and down-dip directions of the CBM reservoir (line AB), three couples of observation points on the symmetry of the well are identified on the line AB, and designated as up_1, dp_1; up_2, dp_2; and u_{p3}, dp_3, respectively, which are located at 30 m, 70 m, and 230 m from the wellbore, respectively. Similarly, along the strike (line CD), three couples of symmetrical observation points are set at symmetrical positions of the production well, which are designated as h_1, h_{11}; h_2, h_{22}; and h_3, h_{33}, respectively. The distances between observation points along the strike are the same as those between points along the dip.
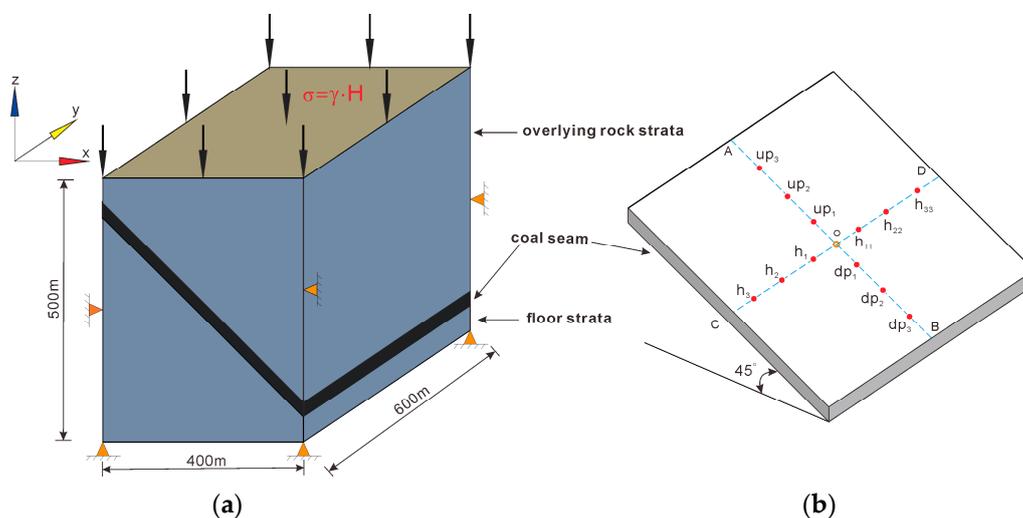

Figure 3. Numerical simulation model, (**a**) simplified geological model, (**b**) model of the coal seam.

Based on the field data and related references, the main input parameters used in this model are listed in Table 1. For this simulation work, the relative permeability curve is one of the important elements. The method of history matching is of practical significance when laboratory data is unavailable [37]. Besides, it might also be the significant practical method to obtain realistic relative permeability values because a relative permeability relationship is measured in a core, these measurements are often not representative of the behavior exhibited by gas and water production from a well, when upscaling laboratory results to reservoir conditions [38]. Therefore, the parameters of the relative permeability curve, which is used in this simulation work, are first obtained by the history matching results, according to the adjacent CS18 well site (data from [15]), and then these parameters are input into the numerical model to predict the production of other wells in the same area (well site 15). Figure 4 shows the comparative result of the curve of *Corey* relative permeability model (Equations (A26) and (A27)) used in this simulation and the actual curve of adjacent well site history matching. Although the *Corey* model curves are not perfectly consistent with the actual relative permeability curves, due to the simple model structure, it might still reflect the in-situ reservoir conditions.

Table 1. Parameters of the numerical simulations.

Parameters and Variables	Values and Units	Acquisition Approach
Thickness	20 m	Field
Desorption time τ	10 days	Experiments
Young's Modulus of coal E	2.19 GPa	Experiments
Poisson's Ratio of coal ν	0.33	Experiments
Initial porosity for coal matrix φ_{m0}	0.06	Experiments
Initial porosity for fracture φ_{f0}	0.005	Experiments
Initial permeability k_{f0}	5.0-0.00125 H/m mD	[16]
Gas dynamic viscosity μ_g	1.84×10^{-5} Pa·s	[33]
Water dynamic viscosity μ_w	1.01×10^{-3} Pa·s	[33]
Density of coal skeleton ρ_s	1400 kg/m^3	[33]
Density of water at standard condition ρ_w	1000 kg/m^3	[33]
Average volume weight of the rock layer	2500 kN/m^3	-
Klinkenberg Factor b	0.15 MPa	[32]
Reference temperature for the desorption tests of the gas T_t	300 K	[33]
Langmuir pressure constant P_L	3.29 MPa	[15]
Langmuir volume constant V_L	0.0157 m^3/kg	[15]
Initial water saturation S_{w0}	0.8	Estimation
Langmuir volumetric strain constant ε_L	0.052	[15]
Endpoint relative permeability of the water k_{rw0}	1.0	History match
Endpoint relative permeability of the gas k_{rg0}	0.85	History match
Irreducible water saturation S_{wr}	0.25	History match
Residual gas saturation S_{gr}	0.15	History match
Capillary pressure p_{cgw}	0.05 MPa	[32]
Molar mass of the methane Mg	16 g/mol	[33]
Standard atmospheric pressure p_s	101 kPa	[33]
Universal gas constant R	8.314 J/(mol·K)	[33]
Temperature under standard conditions Ts	273.5 K	[33]
Reservoir pressure gradient	1 MPa /100m	[16]
Well diameter	0.1 m	Field
Bottom hole pressure	0.2 MPa	Field
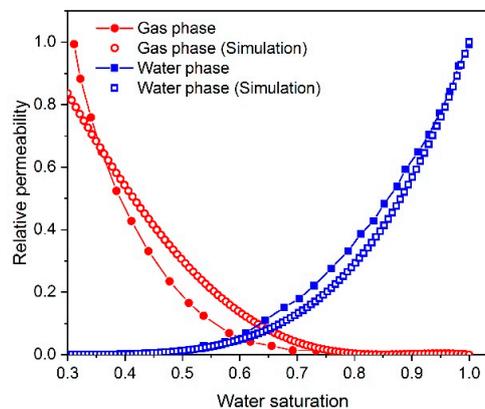
Figure 4. Relative permeability curve for history matching and simulation project.

3.2. Results and Analysis

3.2.1. Production Profile Characteristics and Model Validation

As production time progresses, the water production rate gradually decreases, while the gas production rate first increases and then decreases, resulting in a stable production stage. The results of the simulation (Figure 5a) show that the water production rate is 30.6 m³/d after 10 days of drainage, and decreases rapidly to 3.2 m³/d at the 200-day point, with a decrease of nearly 90%. The water production rate is only 0.19 m³/d after 400 days of drainage, and almost 0 after 500 days. Unlike the traditional horizontal unconventional gas reservoirs, the gas production characteristics of the steeply-dipping reservoirs are known to be characterized by "dual peaks". The gas production rate is 814 m³/d at the 10-day drainage point, and increases sharply to 7837 m³/d at the 200-day point, achieving an increase of 980%. It is found that the gas production rate reaches the first peak of 7997 m³/d after 250 days, then begins to decline slightly, reaching an inflection point of 7641 m³/d at the 350-day point. Then the gas production begins to rebound. The second peak of 8132.6 m³/d is reached after 400 days of drainage, which corresponds to the extremely low water production rate at that time. After reaching the second peak, the gas production rate gradually decreases, and finally stabilizes at approximately 7082 m³/d. Unsurprisingly, the simulated gas production in Figure 5a is not perfectly consistent with the actual production, shown in Figure 5b, especially for the later production stage. This might be mainly attributed to coal failure and anisotropic permeability. Coal failure can result from reservoir pressure depletion (later production stage), due to the coupled effect of increasing vertical effective stress and the decreasing horizontal effective stress. The enhanced production of coal solids and fines might accompany by a potential permeability decrease, due to fines creation, movement, and plugging; thus, it would reduce gas production. Besides, for the thinner CBM formations, the vertical permeability is almost negligible, due to the dominant horizontal flow, while the effect of vertical permeability might be more pronounced in the cases of ultra-thick coal seams. The assumption of isotropic permeability in this simulation project might result in an overestimation in actual gas production. Note that, compared with the values of gas and water production rate, we are more concerned about the specific shape of simulated gas production profile, i.e., "dual-peak", for steeply-dipping coal reservoirs. This characteristic is consistent with the actual production profile in Figure 5b and previous research in Figure 6. These results indicate that the model is reasonably effective for examining the CBM extraction in steeply-dipping reservoirs. Therefore, based on simulation results in this study, the depressurization, permeability evolution, and fluid saturation distribution of the examined reservoir could be further analyzed.
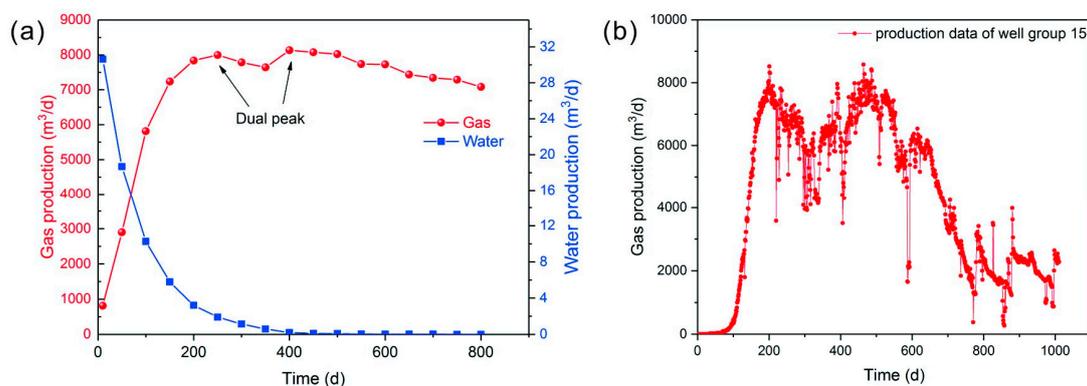

Figure 5. Production profile characteristics, (**a**) numeric simulation results of the water and gas production rates, (**b**) gas production profile for the well group 15 in Fukang Mining Area.
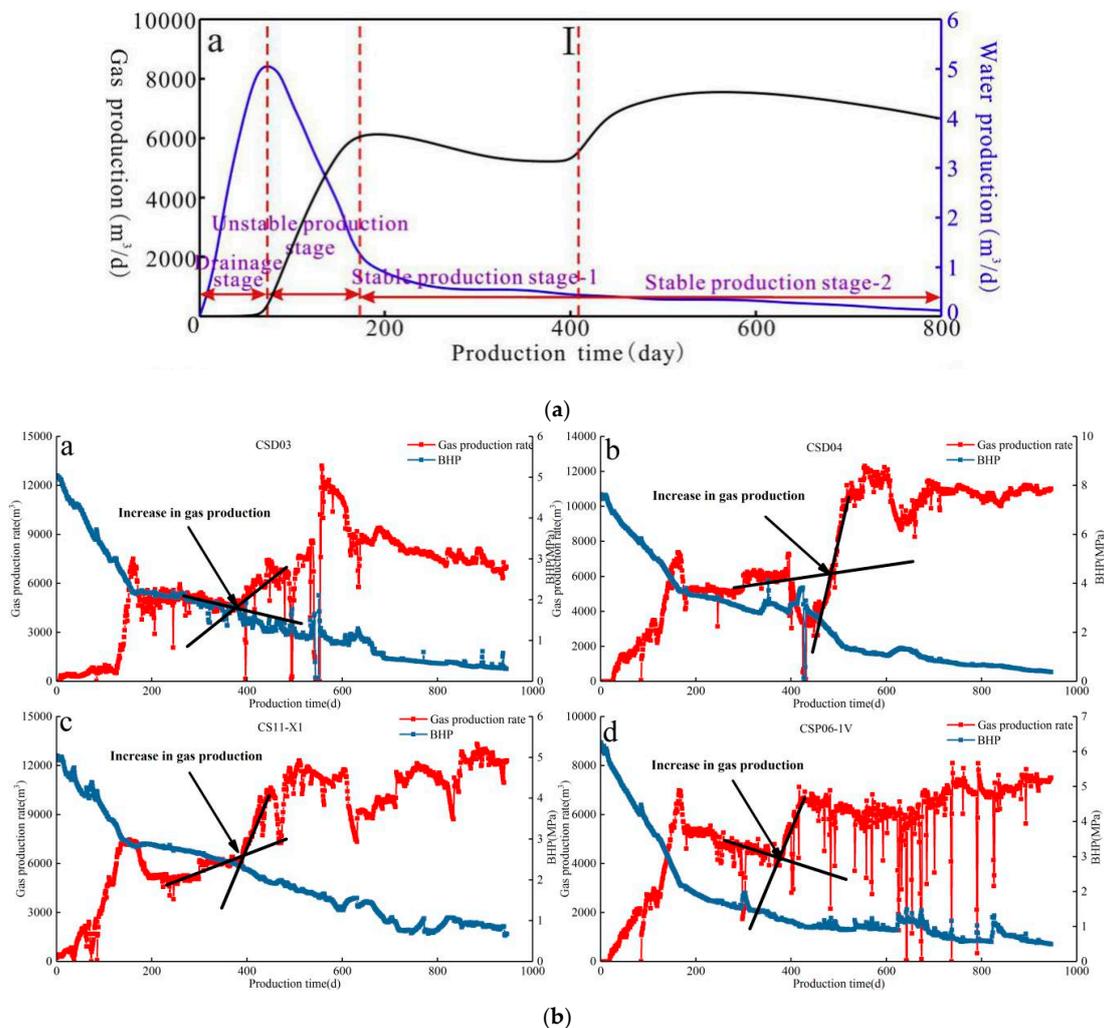
(a)

(b)

Figure 6. Production rate curves from previous research projects, (**a**) water and gas production profiles of steeply-dipping reservoirs in the west Fukang Block [16], (**b**) gas production profiles for four CBM wells of well site 11 of the Fukang western block [39].

In regard to the "dual peaks" appearing on the gas production curves of steeply-dipping and thick coal reservoirs, it is presumed that the asymmetric changes in the gas and water production rates in the upper and lower sections of the reservoirs are the cause. In other words, due to the asynchronous changes in gas production rates in the upper and lower directions of the reservoirs, there are time differences between the two peak values during certain periods of time. When gas production rate curves have the opposite monotonicity, and the change rates appear to be different in the upper and lower directions of the reservoir, the total production rate curves may present as inflection points and display two peaks. In terms of the water production curves, although the upper and lower directions of water production curves are not exactly the same, they both show monotonous decreasing trends, and the water production rates are much lower than the gas production rates. Therefore, the total water production curves remain exponentially decreasing, and there are no inflection points observed. This type of phenomenon (Figure 5a) has also been observed and reported [15,16]. Recently, the Eclipse numerical simulation is employed to investigate the characteristics and differences of gas production for CBM reservoirs with different dip angles [39]. The simulation results show that CBM wells in a steeply inclined reservoir exhibit a "dual-peak" shape-gas production profile. To further confirm the gas production profile characteristics for a steeply-dipping reservoir, Kang et al. (2019) [39] selected four CBM wells in shallow reservoirs (burial depth of approximately 650 m) of well site 11 of the Fukang western block as the field production cases. The main reason is that they are all single-layer

production wells, which can eliminate interference caused by multiple layer asynchronous production. Although the gas production profile is not as smooth as those given by the simulation results, it can be clearly observed that after initial gas production declines for some time, a substantial increase in gas production occurs, and the gas production profile forms a concave point. This finding also confirms the "dual peak" features of the gas production profile of a steeply inclined reservoir in terms of numerical simulations and actual production (Figure 6b).

3.2.2. Evolution of the Depressurization

Unlike horizontal reservoirs, the initial reservoir pressure differences (Figures 7 and 8), which exist in the steeply-dipping coal reservoirs before drainage (for example, the initial reservoir pressure rates in the up-dip and down-dip directions of the reservoirs) tend to be different. Since the main driving force of reservoir drainage is the pressure gradient between the reservoir fluids and the bottom holes of production wells, the characteristics of the reservoir depressurization in the up-dip and down-dip directions will vary, as detailed in Figures 7–10. In addition, due to the different densities of the gas and water, the gas-water gravity differentiations are also one of the factors affecting the asymmetric distributions of the pressure drops.
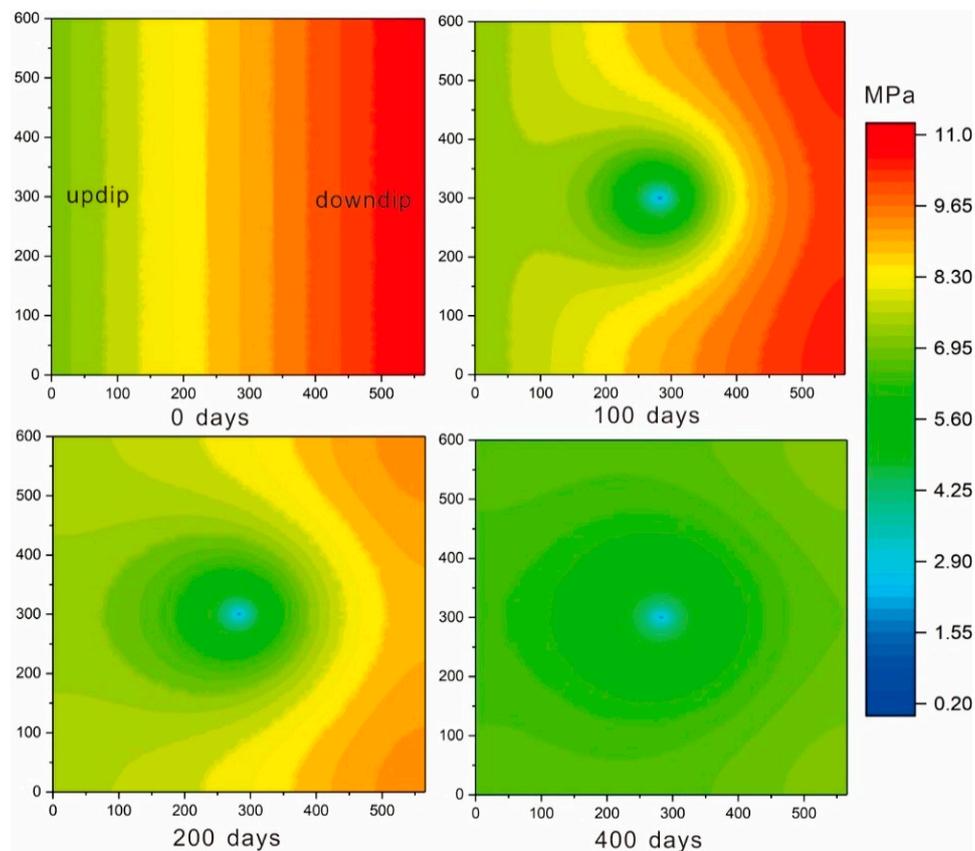

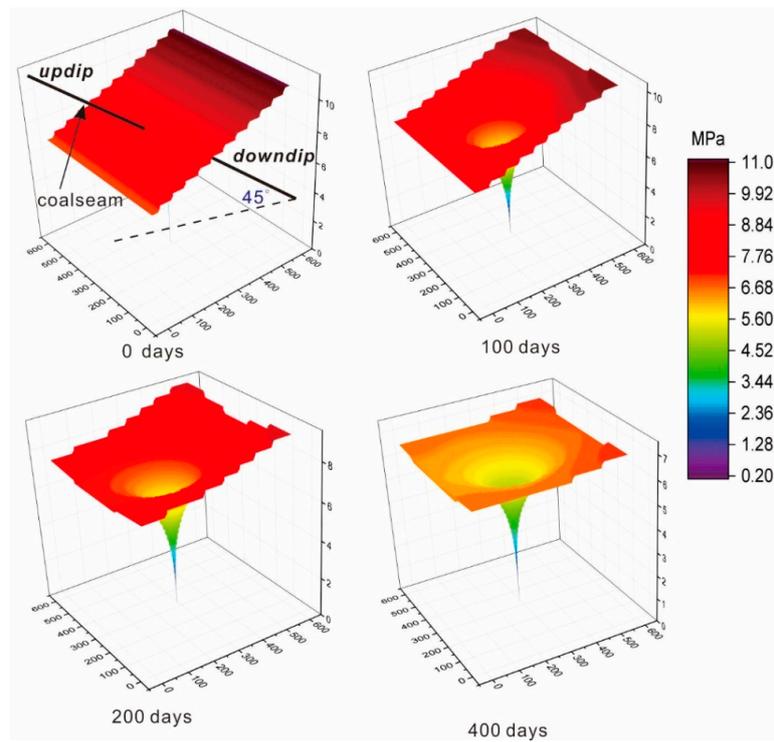**Figure 7.** Nephogram of the reservoir pressure distribution (vertical view).

Figure 8. Evolution of the reservoir depressurization funnel during CBM extraction.
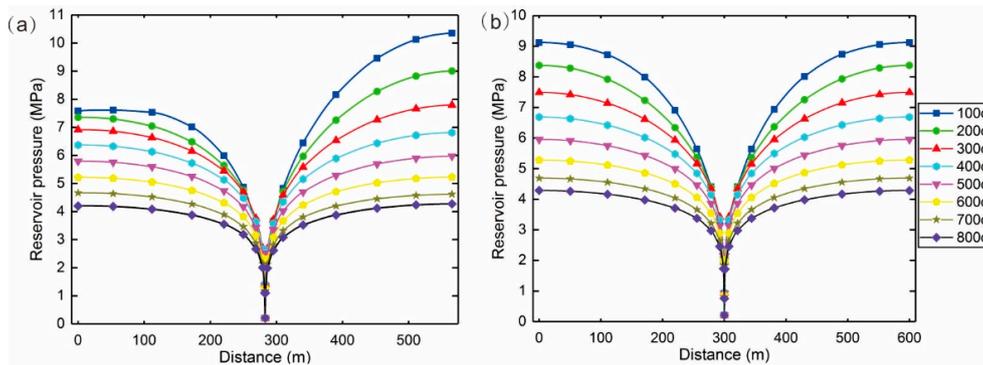

Figure 9. Distribution of the reservoir pressure, (**a**) along the reference line AB (the dip), (**b**) along the reference line CD (the strike).
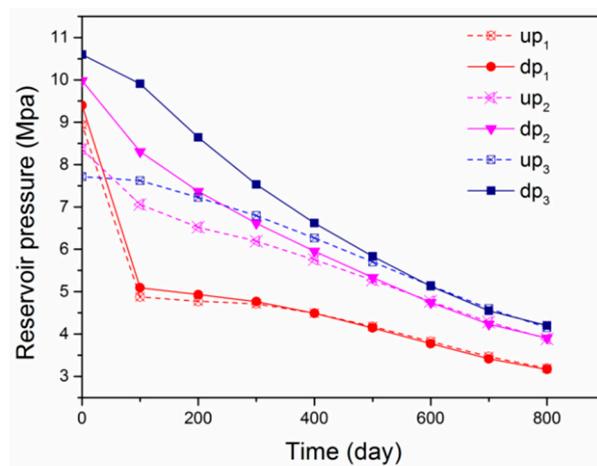

Figure 10. Pressure evolution of the reservoir at different points.

It is observed in this study that during the early stage of drainage and production (<100 days), the reservoir pressure levels drop sharply near the production well (along the coal seam dip with a distance of 30 m; points up_1 and dp_1). The initial reservoir pressure at point up_1 is 8.9 MPa, and drops to 4.87 MPa after drainage for 100 days, i.e., a drop of 45.2% (Figure 10; Table 2). The initial reservoir pressure at point dp_1 is 9.4 MPa, and decreased to 5.09 MPa after 100 days, with a corresponding depressurization of 45.8%. While for farther points up_2 and dp_2, 70 m away from the well along the dip, the depressurization is smaller. The initial pressures for points up_2 and dp_2 are 8.36 and 9.98 MPa, respectively, which separately changed to 7.05 and 8.30 MPa (reduction of 15.6% and 16.8%) after 100 days. For the farthest observation points up_3 and dp_3 (230 m away from the well along the dip), the initial pressure is 7.71 and 10.6 MPa, which decreases to 7.62 and 9.91 MPa, respectively, after 100 days of drainage (with depressurization of 1.16% and 6.5%). Obviously, it is observed that the depressurization along the down-dip is larger than that along the up-dip during the initial drainage stage. In addition, it is found that the farther away from the wellbore the area is, the greater the differences in depressurization between the up-dip and down-dip direction with the same distance away from the wellbore would be.

Table 2. Pressure distributions of the reservoir at different observation points during production.

Observation Point	Initial Pressure/MPa	100 Days	Percentage Change	400 Days	New Percentage Change I	800 Days	New Percentage Change II
up_1	8.9	4.87	−45.2%	4.49	−7.8%	3.18	−29.2%
dp_1	9.4	5.09	−45.8%	4.48	−11.9%	3.16	−29.4%
up_2	8.36	7.05	−15.6%	5.75	−18.4%	3.88	−32.5%
dp_2	9.98	8.30	−16.8%	5.95	−28.3%	3.91	−34.3%
up_3	7.71	7.62	−1.16%	6.26	−17.8%	4.14	−33.9%
dp_3	10.6	9.91	−6.5%	6.62	−33.1%	4.19	−36.7%

With the advancement of drainage (100 to 400 days), the reservoir depressurization continued to spread to distant locations. The reservoir pressures at observation points up_1 and dp_1 are 4.49 and 4.48 MPa, respectively, after drainage for 400 days, which are, respectively, 7.8% and 11.9% lower than that after drainage for 100 days. For points up_2 and dp_2, which is located in the middle of up-dip and down-dip directions, the pressure is 5.75 and 5.95 MPa separately, with the corresponding decline of 18.4% and 28.3%, after 400 days of drainage. As for the edge points up_3 and dp_3 along the up-dip and down-dip directions, the reservoir pressure is separately 6.26 and 6.62 MPa after 400 days (with each descent of 17.8% and 33.1%). It is observed that during the mid-term stage of drainage and production, the depressurization in the down-dip direction have remained consistently greater than that in the up-dip direction. Also, the differences in the depressurization values are found to be more obvious with larger distances from the production well.

It is founded that during the later stage of drainage (>800 days), the reservoir depressurization continued to spread to more distant areas. After drainage for 800 days, the reservoir pressure at point up_1 is 3.18 MPa, or a continued decrease of 29.2%. The reservoir pressure at point dp_1 is determined to be 3.16 MPa, with a new drop of 29.4%. For the farther points up_2 and dp_2, the reservoir pressure continues to decline to 3.88 and 3.91 MPa, respectively, after drainage for 800 days (with each drop of 32.5% and 34.3%). For the farthest points up_3 and dp_3, after 800 days, the reservoir pressure separately drops to 4.14 and 4.19 MPa, with declines of 33.9% and 36.7% for each. Obviously, the results show that during the later production stage, the reservoir pressure continues to drop along the up-dip and down-dip, and tends to have similar reduction rates near the production well. However, for areas farther away from the well along the dip, the observed decline in reservoir pressure in the up-dip direction is slightly smaller than that along the down-dip. It should be noted that the gravity differentiation characteristics have not been found to be significant. In summary, after drainage for 800 days, the initial pressure differences within the reservoir have almost disappear, and the reservoir pressure of each couple of symmetrical points are very close. The depressurization profiles of the

reservoir are found to be similar to that of a horizontal reservoir, and are symmetric regarding the production well (normal direction of the reservoir).

It is found that the depressurization propagation process of steeply-dipping coal reservoirs presents special temporal and spatial characteristics compared with horizontal reservoirs. Specifically, it is observed that during the initial drainage stage, the depressurization near the well is fast and approximately synchronous. It is surmised that the gap between reservoir pressure around the drainage well and the bottom hole pressure might make the initial reservoir pressure difference along the dip and gravity influence negligible. This finally results in an approximately symmetrical change (decrease) in the reservoir pressure around the well. However, as the distance away from the production well increases, the effects of the reservoir pressure difference in the up-dip and down-dip directions intensify. For example, the maximum difference value of depressurization could be 15.3% for the farthest symmetric points (up$_3$ and dp$_3$) after 400 days. Moreover, after 800 days, the initial reservoir pressure difference within the reservoir essentially disappear and could be neglected. The pressure values of a couple of the symmetric points along the dip tend to be the same, and the distribution of the reservoir pressure gradually resembles that observed in horizontal reservoirs.

3.2.3. Evolution of the Permeability

Similar to the finding of previous studies, in the process of drainage and production, the effective stress and matrix shrinkage have alternately become the dominant factor for permeability evolution. The permeability first decreases, and then rebounds (Figure 11). The different distribution of the reservoir permeability along the dip of the reservoir is one distinct difference between the flat and incline reservoirs. The permeability evolution of steeply-dipping reservoirs demonstrates space-time effects. Along the dip of the reservoir, the effective stress dramatically increases as the reservoir pressure sharply decreases at the initial stage of CBM recovery. The permeability of a couple of points decreases almost synchronously. A reduction of up to 60% from the initial permeability is observed after drainage for 20 days (Figure 11a). Next, due to the positive effects of the matrix shrinkage, the decrease rates of permeability for points up1 and dp1 decelerate; however, the effective stress still dominates the evolution of reservoir permeability. After ~180 days, the permeability at points up$_1$ and dp$_1$ rebounds, and the permeability ratio at these two points decreases to 0.49 and 0.46, respectively. Subsequently, the matrix shrinkage begins to dominate the permeability evolution, and the permeability increases gradually. The permeability at these two points is, respectively, 1.26 and 1.2 times that of the initial values at 800 days.
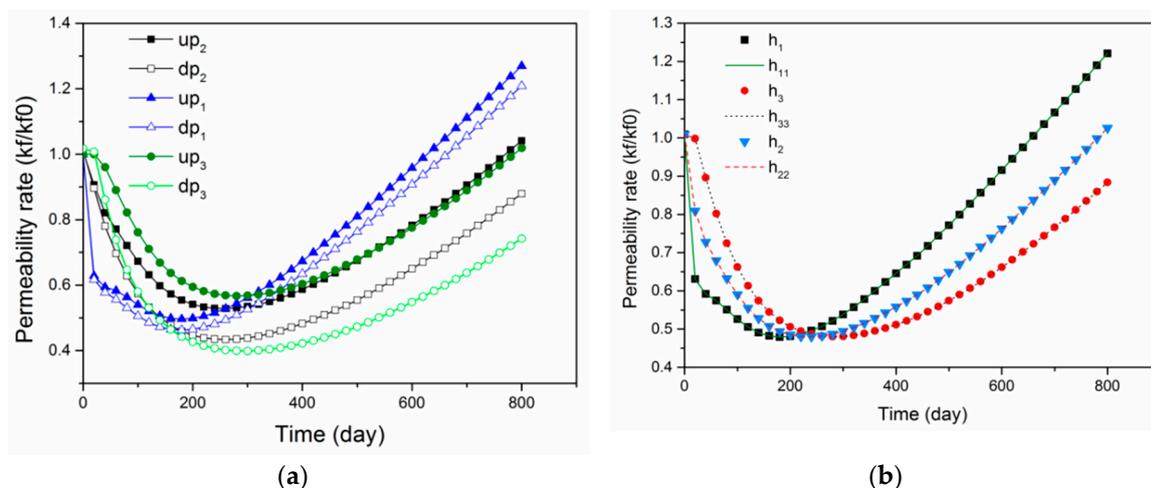

Figure 11. Coal permeability evolution at different points, (**a**) points located on line AB (along the dip of the reservoir), (**b**) points located on line CD (along the strike).

It is worth noting that the rebound permeability at point dp_1 is lower than those at other points along the up-dip (up_1, up_2, and up_3 points). This could be attributed to the more significant negative effects of the effective stress at that location (dp_1). On the other hand, due to the strong matrix shrinkage around the well, along with the gas slippage under the lower reservoir pressure, coal permeability around the well has greatly increased, which ultimately even exceeds the permeability at points up_2 and up_3. In regard to points up_2 and dp_2, the permeability firstly decreases. While due to the rapid decline of reservoir pressure and the larger in-situ stress in the lower section of the reservoir, the negative effects of effective stress at point dp_2 are stronger than those at point up_2. The permeability at points up_2 and dp_2 separately decrease to 52.8% and 43.4% of the initial values after draining for 260 days. Then, the matrix shrinkage begins to dominate the permeability evolution. The permeability growth rates of these two points are almost the same during the later drainage stage (Figure 11a). Due to the negative effects of the effective stress on permeability during the initial drainage stage, the final permeability at point up_2 is still higher than that at point dp_2, which are separately 1.04 and 0.87 times that of the initial values. For the farthest points up_3 and dp_3, the significant differences in the in-situ stress and reservoir depressurization between them result in a difference in the effective stress. The effective stress at the lower point dp_3 is much larger than that at, the higher point up_3. Therefore, the negative effects of the effective stress on the permeability of the lower section of the reservoir is stronger, of which the rebound point of the permeability profile emerges later (280 days for point up_3, and 300 days for point dp_3). The corresponding permeability decreases are separately 56.6% (point dp_3) and 38.8% (point up_3) versus the original permeability. After the rebound point of permeability evolution, the permeability gradually increases as CBM recovery proceeds (Figure 11a).

Along the strike of the coal seam, the permeabilities of all points first decrease and then rebound as production continues (Figure 11b). Spatially, different from points along the dip, permeabilities of each couple of the symmetrical points along the strike synchronously change during the CBM recovery. At symmetrical locations, the in-situ stress distribution and reservoir depressurization evolution are synchronous (regarding the well), and the same in the magnitude, which leads to the permeability changes synchronously (Figure 12b). The increases in permeability after the rebound point are mainly dependent on the degree of the matrix shrinkage.
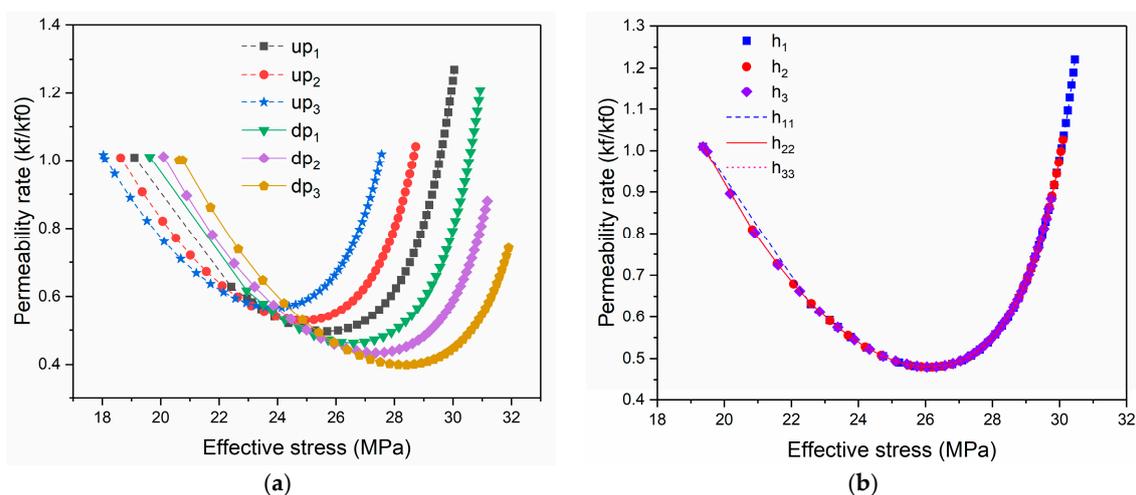

Figure 12. Relationship between the effective stress and the permeability: (**a**) Points located on line AB (along the dip of the reservoir), (**b**) points located on line CD (along the strike).

In brief, from the perspective of time, the asymmetric permeability evolution along the dip of the steeply-dipping reservoir is controlled by the negative effects of effective stress and the positive effects of matrix shrinkage, which alternately becomes the dominant factor during the whole production. From a spatial aspect, due to the asymmetry of the in-situ stress distribution and reservoir depressurization along the dip, the negative effects of the effective stress on permeability within the upper section are

weaker than those within the lower section (Figure 12a). The negative effects of the effective stress at locations far from the drainage well play a major role in controlling the evolution of permeability.

3.2.4. Distribution of the Fluid Saturation

Unlike the single-phase seepage, in the study of two-phase seepage, the distribution of fluid saturation is another key issue that need to be investigated. Fluid saturation affects the migration of gas and water in coal seams by controlling the relative permeability. The distribution of water saturation in the steeply-dipping CBM reservoir is different from that in the horizontal reservoir (Figures 13–15). In the vicinity of the well, taking points up_1 and dp_1, for example, the water saturation changes synchronously, and the magnitudes are approximately the same throughout the whole drainage process. While for the farther areas along the dip, such as the symmetrical points up_2 and dp_2, or up_3 and dp_3, during the initial drainage stage (<100 days), the magnitudes of water saturation in the lower section (dp_2/dp_3) and upper section (up_2/up_3) are also almost the same. During the mid-term stage of drainage (100–700 days), water saturation levels in the lower section are slightly larger than those in the upper sections, and get close again at the final stage (>700 days) (Figure 15).
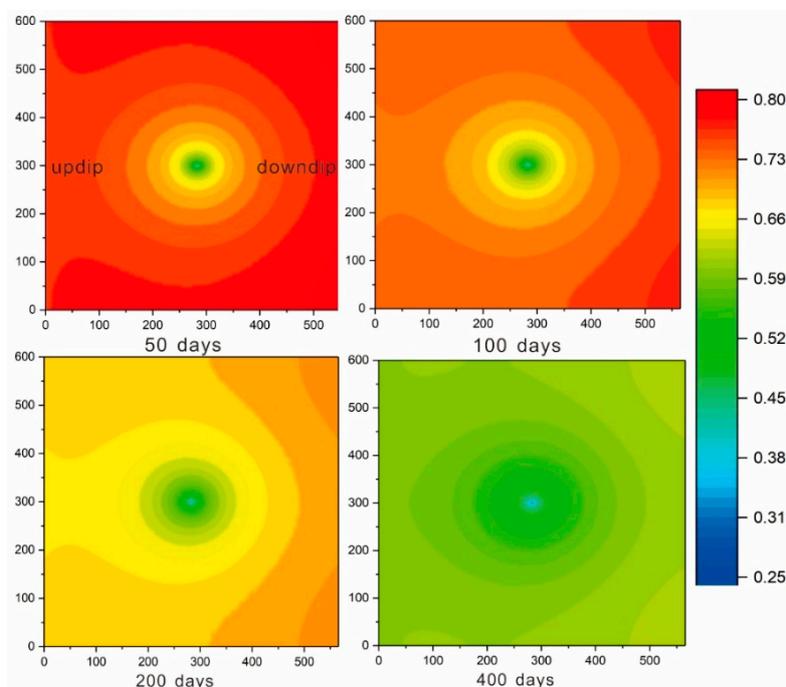

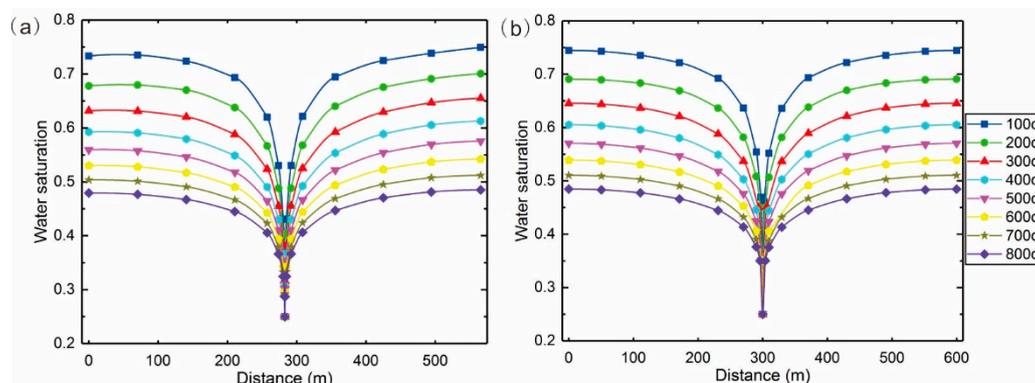**Figure 13.** Nephogram of the water saturation distribution (vertical view).

Figure 14. Distribution of the fluid saturation along the reference lines, (**a**) reference line AB (along the dip of the reservoir), (**b**) reference line CD (along the strike).
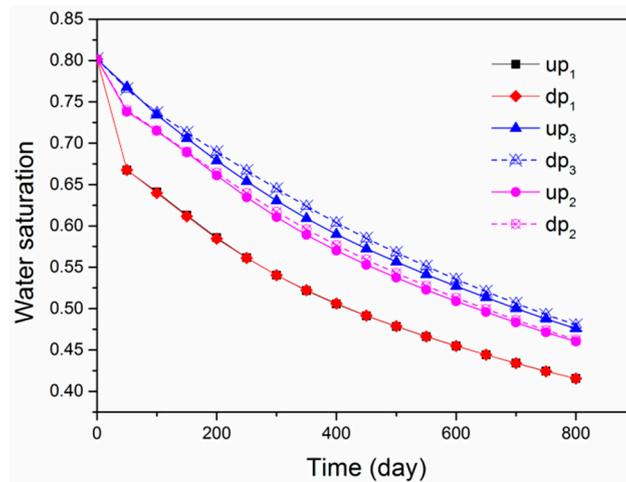
Figure 15. Evolution of water saturation at the three couples of points along the dip.

In summary, it is indicated that the drainage pressure gradient, as the driving force of darcy seepage, is larger near the well in the early stage of drainage, and plays a dominant role in the process of water transport in fractures. The influence of fluid gravity could be neglected, since the water saturations in the up-dip and down-dip directions change almost synchronously throughout the whole drainage process. Due to the larger differential pressure between the lower section of the reservoir and drainage well, it is favorable for dewatering and depressurization in the lower section. However, as the reservoir pressure along the dip decreases, more deep water would migrate to the bottom of the well, which results in higher water saturation in the down-dip direction versus that in the up-dip direction. The difference in water saturation admonishes as the initial reservoir differential pressure depletes, and the final distribution of water saturation is similar to that in the horizontal reservoir (a symmetrical distribution with respect to the well along the dip).

4. Discussion

A coupled mathematical model, which considers gas and water gravity and two-phase flow, is established. The results are detailed in Table 3. The conclusions obtained in this study are similar to those presented by References [15,16], especially, for the "dual peaks" characteristics of gas production profiles. Furthermore, the results also indicate that the differences in the initial physical parameters between the deep and shallow reservoirs are the main reason which leads to the asynchronous evolution of the reservoir pressure, permeability, and water saturation, as well as the appearance of "dual peaks" in the evolution of gas production.

Table 3. Different referenced studies regarding CBM extraction in the steeply-dipping reservoirs.

Study Conducted by	Coupled Model	Depressurization	Permeability Evolution	Fluid Saturation Distribution	Production Characteristics
[13]	×	√	×	×	×
[14]	√	√	×	×	×
[15]	×	√	×	×	√
[16]	×	√	×	×	√
The present study	√	√	√	√	√

Regarding the transport characteristics of steeply-dipping reservoirs, some previous studies have discussed the practicability of application for well types (e.g., horizontal wells or U-shaped wells), well space, and well location selection [17,40]. Based on the obtained results, this study proposes the following suggestions for well layout optimization and ECBM methods:

(1) To shorten the dewatering period and to decrease water saturation at the lower section of the reservoir, cluster well groups are suggested to be utilized in the extraction of steeply-dipping UTCBM

reservoirs. Meanwhile, the density of the well pattern in the lower section of the reservoir would be appropriately greater than that in the upper section.

(2) Changes in permeability along the dip are more strongly affected by effective stresses, resulting in asymmetry relative to the production wells, particularly in locations far away from the wells. The permeability at downdip direction sharply decreases, due to the larger effective stress. Thus, N_2 enhanced CBM stimulation technology is suggested to be utilized in the extraction of steeply-dipping CBM reservoirs. Note that the injection well should be set in the lower section of the reservoir; in contrast, production well should be set in the upper section. Injectant of N_2 could reduce the CH_4 partial pressure in the cleats, as an added benefit, it can also sustain the positive effects of a higher total reservoir pressure on permeability in-depth reservoir to moderate the severe permeability loss, and accelerate the gas flow rate by adding the additional driving force.

The evolution of production and transport characteristics of steeply-dipping UTCBM reservoirs have been revealed, which are mainly attributed to the geological characteristics related to the large dip angles. However, the results fail to accurately reflect the influences of such characteristics as the "ultra-thick and low-rank coal seams" during the CBM extraction. The limitation of the existing isotropic permeability model, which is commonly adopted in numerical simulation, results in this failure. Actually, coal is one kind of typically anisotropic material, including permeability and mechanical properties, particularly in the cases of low-rank coal seams [41,42]. Figure 16 shows that the aperture sizes of the cleats (face and butt cleats) and structure of bedding planes, which potentially cause the permeability anisotropy. According to the field and laboratory test, it has been confirmed that the horizontal permeability is often larger than that in the direction of the vertical bedding planes [43,44]. Recent experimental research has reported the properties of anisotropic permeability of low-rank coal samples in Fukang Mining area, which indicates that the Hellum permeability decreases from the face cleat direction to the butt cleat direction, and then perpendicular to the bedding direction, with a maximum ratio of the three directions reaching approximately 10.98:4.69:1 [42]. For the thinner CBM formations, the vertical permeability is almost negligible, due to the dominant horizontal flow [43], while the effect of vertical permeability might be more pronounced in the cases of ultra-thick coal seams [20]. Therefore, it is necessary to further investigate the anisotropic permeability models of coal in accordance with the actual conditions of low-rank and ultra-thick coal seams.
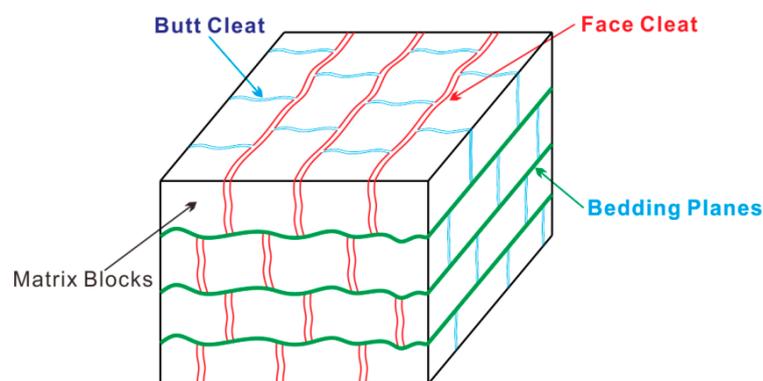

Figure 16. Anisotropic structure of coal.

5. Conclusions

The following conclusions are drawn with regard to the special response of steeply-dipping ultra-thick coal bed methane reservoirs:

(1) These reservoirs exhibit a "dual peaks" in methane flow rates in time. This results from a rapid drop in water saturation from high water production rates in the upper reservoir, complemented by a substantial increase in gas production rate. However, following a stable production period, the gas production rate does not decline, as commonly observed in horizontal or near-horizontal reservoirs, as it is affected by the asynchronous and constructive interference of changes in gas production rates in

the upper and lower dip areas. Declines in gas production in the upper reservoir are complemented by delayed rate increases in the deep reservoir that then also slowly decay to a second stable production rate plateau.

(2) During initial drainage, the drop in reservoir pressure in the up-dip and down-dip directions near the production wells are rapid and change both synchronously and symmetrically. However, distant from the drainage wells, this synchronicity and symmetry are broken. Declines in reservoir pressure are affected by the initial reservoir pressure differences at locations far from the wells. Moreover, the pressure drops in the down-dip direction are much higher than those in the up-dip direction—with this effect disappearing in late times where drawdown resembles that of standard horizontal reservoirs.

(3) The absolute permeability of steeply-dipping coal reservoirs is strongly controlled by effective stresses and the matrix shrinkage impacting permeability evolution. However, the relative and respective influence of these two factors differ. Changes in permeability along strike are more strongly affected by matrix shrinkage, while effective stresses exert principal control in the up-dip and down-dip directions, resulting in asymmetry relative to the production wells, particularly in locations far away from the wells.

(4) Buoyant effects near the production wells cannot be ignored. Although water saturation changes almost synchronously in the up-dip and down-dip directions, but with the down-dip direction having a higher pressure gradient. Recovery of the incompressible water from the down-dip reservoir results in a larger gas pressure differential that then drives elevated production. Similarly, it is difficult to achieve an effective supply in the upper reservoir, although these differences gradually decrease with the disappearance of the initial reservoir pressure differences. Again, the saturation distribution of the steeply-dipping reservoir finally reverts to that similar to traditional horizontal reservoirs.

(5) Differences in the initial geological characteristics (in-situ stress, initial reservoir pressure, and permeability) between the deep and shallow regions results in the asynchronous evolution of reservoir pressure, permeability, fluid saturation, and a "double peak" feature in gas production rate. The foregoing has emphasized the fundamental reasons why steeply-dipping CBM reservoirs differ from horizontal reservoirs. Fluid gravity exerts little effect on fluid migration, principally since buoyant effects are only important in the intervening period of desaturation, which is short-lived. Otherwise, the impacts of permeability evolution are so large that they dominate behavior, due to the dual effects of matrix shrinkage (along-strike) and effective stresses (down-dip).

Author Contributions: X.F., D.E., X.L. (Xuehua Li) and S.L. conceived and designed the numerical simulation scheme. S.L. and H.H. performed the numerical simulation software and analyzed the data. Q.Y., J.K. and X.L. (Xin Li) helped S.L. analyze the data. X.L. (Xin Li) and J.K. supported the research in terms of both scientific and technical expertise. S.L. and H.H. wrote the original draft. D.E. and X.L. (Xuehua Li) helped S.L. revise the manuscript. All authors have read and agreed to the published version of the manuscript.

Appendix A.

Appendix A.1. Governing Equations

Appendix A.1.1. Governing Equation of the Hydraulic Field

Independent variables of the seepage field are represented in 4D (x, y, z, and t) via the dependent variables of fluid pressure and saturation. The representative elemental volume (REV) includes

fractures and coal matrix with the equation for the mass balance of the water and gas two-phase flow in the REV defined as:

$$\frac{\partial m}{\partial t} + \nabla \cdot \left(\rho_p v_p \right) = Q_s \tag{A1}$$

where ρ_p is the gas or water density, kg/m^3; v_p indicates the Darcy velocity of the gas or water phase, m/s; t denotes the time, s; Q_s is a source term, kg m^{-3} s^{-1}; and m indicates the methane or water content, kg/m^3.

The methane content in the REV comprises both free-phase gas in the fractures (m_{fg}) and matrix pores (m_{mg}) and adsorbed gas content (V_{sg}), and is expressed as:

$$m_g = m_{fg} + m_{mg} + \rho_c \rho_{gs} \left(1 - \varphi_f \right) V_{sg} = \rho_{fg} \varphi_f S_g + \rho_{mg} \varphi_m + \rho_c \rho_{gs} \left(1 - \varphi_f \right) V_{sg} \tag{A2}$$

where ρ_c is the coal density, kg/m^3; ρ_{gs} represents the gas density under standard conditions; $V_{sg} = V_L p_m / (p_m + P_L)$ is the absorbed methane content, m^3/kg; φ_m indicates the porosity in the matrix; φ_f denotes the fracture porosity; S_g indicates the gas saturation; ρ_{fg} is the free gas density within the fractures, m^3/kg; ρ_{mg} represents the free gas density in the matrix micro-pores, m^3/kg; p_m is the gas pressure in the matrix, Pa; and V_L and P_L are the Langmuir volume (m^3/kg) and pressure (Pa) constant, respectively.

Then, the water content in the REV can be expressed as follows:

$$m_w = \rho_w \varphi_f S_w \tag{A3}$$

where ρ_w is water density; and S_w is water saturation, $S_w + S_g = 1$.

The reservoir pressure is defined as [27,32]:

$$p_f = S_g p_{fg} + S_w p_{fw} \tag{A4}$$

where p_{fg} is gas pressure in the fractures, Pa; and p_{fw} indicates the water pressure in the fractures, Pa.

Therefore, the relationship between the gas pressure and water pressure can be expressed as:

$$p_{cgw} = p_{fg} - p_{fw} \tag{A5}$$

where p_{cgw} is the capillary pressure, Pa.

Then, according to the ideal gas law, the gas density can be described as:

$$\rho_{fg} = \frac{M_c}{RT} p_{fg} \tag{A6}$$

$$\rho_{mg} = \frac{M_c}{RT} p_m \tag{A7}$$

where M_c is the molar mass of the methane, g/mol; R is the universal gas content, J/(mol·K); and T is the temperature, K.

Buoyancy is considered for both gas and water, defining Darcy's law for two-phase flow in the fractures as:

$$v_g = -\frac{k_{eg}}{\mu_g} \left(\nabla p_f + \rho_g g \nabla z \right) \tag{A8}$$

$$v_w = -\frac{k_{ew}}{\mu_w} \left(\nabla p_f + \rho_w g \nabla z \right) \tag{A9}$$

where the subscripts g and w refer to the gas and water, respectively; v_g and v_w indicate the Darcy Law velocity of the gas and water, respectively, m/s; μ_g and μ_w denote the dynamic viscosity; k_{eg} and k_{ew} are the effective permeability of the gas and water, respectively, m^2; ∇z is the gravitational term; and g indicates gravitational acceleration, m/s^2.

Desorption and diffusion play important roles in CBM production due to the large portions of adsorbed gas in the coal matrix. The depressurization of CBM reservoirs is directly controlled by dewatering of the fracture system. Meanwhile, the mass exchange between matrix and fractures are dominated by diffusion. In-situ CBM is in a dynamic equilibrium in which the gas pressure in the matrix is equal to the reservoir pressure in fractures—with this equilibrium disturbed by the dewatering [45]. The mass flux may be defined as [46,47]:

$$q = -\frac{\partial m_{mg}}{\partial t} = D\sigma_c\left(\rho_{mg} - \rho_E\right) = D\sigma_c\frac{M_c}{RT}(p_m - p_E) \tag{A10}$$

where q is the gas exchange rate between the matrix and the fractures, kg/(m³·s); and $m_{mg} = \rho_{mg}\varphi_m + \rho_c\rho_{gs}V_{sg}$ is the mass of methane in the coal matrix, kg/m³; where σ_c indicates the coal matrix block shape factor, m⁻²; D is the gas diffusion coefficient, m²/s; ρ_{mg} indicates the concentration of gas in the matrix blocks, kg/m³; and ρ_E denotes the equilibrium concentration between the matrix and the fractures, kg/m³. We use adsorption time to estimate the effective gas diffusion coefficient in the coal matrix as [48]:

$$\tau = \frac{1}{D\sigma_c} \tag{A11}$$

where τ is the sorption time of the coal matrix, which is numerically equivalent to the time for 63.2% of the coal gas to be recovered, s.

Reservoir pressure p_f is defined as [27]:

$$p_E = \frac{RT}{M_c}\rho_c\rho_{gs}\frac{V_L p_f}{p_f + P_L} \tag{A12}$$

Enabling the substitution of Equations (A11) and (A12) into Equation (A10), to return the governing equations of the diffusion field as:

$$-\frac{\partial p_m}{\partial t}\left(\frac{M_c}{RT}\varphi_m + \rho_c\rho_{gs}\frac{V_L p_L}{(p_m + p_L)^2}\right) - \frac{\partial \varphi_m}{\partial t}\frac{M_c}{RT} = \frac{1}{\tau}\frac{M_c}{RT}(p_m - p_E) \tag{A13}$$

so far, ignoring the impact of deformation of the matrix micro-pores, $\partial\varphi_m/\partial t = 0$;

Finally, by substituting Equations (A2), (A3), (A8) and (A9) into Equation (A1), the governing equations of two-phase flow are obtained as:

$$\frac{\partial}{\partial t}\left(\frac{M_c}{RT}P_{fg}\varphi_f S_g + \frac{M_c}{RT}p_m\varphi_m + \rho_c\rho_{gs}\left(1 - \varphi_f\right)\frac{V_L p_m}{p_m + P_L}\right) = \nabla\cdot\left(\frac{M_c}{RT}P_{fg}\frac{k_{eg}}{\mu_g}\left(\nabla p_f + \rho_g g\nabla z\right)\right) \tag{A14}$$

$$\frac{\partial}{\partial t}\left(\rho_w\varphi_f S_w\right) = \nabla\cdot\left(\rho_w\frac{k_{ew}}{\mu_w}\left(\nabla p_f + \rho_w g\nabla z\right)\right) \tag{A15}$$

Combining Equations (A14)–(A16), defines the governing equation of the transport field.

Appendix A.1.2. Governing Equation of the Mechanical Field

For a homogeneous, isotropic, and elastic medium, the strain-displacement relationship and the equilibrium equation can be expressed as follows:

$$\varepsilon_{ij} = \frac{1}{2}\left(u_{i,j} + u_{j,i}\right) \tag{A16}$$

and

$$\sigma_{ij,j} + f_i = 0 \tag{A17}$$

where ε_{ij} represents the strain tensor, $(i, j = 1, 2, 3)$; u_i is the displacement within the element; σ_{ij} is the total stress tensor; and σ_{ij}^e is the effective stress tensor.

The constitutive relationship of an isotropic linear poro-elastic continuum is expressed as [49]:

$$\varepsilon_{ij} = \frac{1}{2G}\sigma_{ij} - \left(\frac{1}{6G} - \frac{1}{9K}\right)\sigma_{kk}\delta_{ij} + \frac{\alpha p_f}{3K}\delta_{ij} + \frac{\varepsilon_s}{3}\delta_{ij} \tag{A18}$$

where $G = E/2(1 + v)$ is the shear modulus, Pa; $K = E/3(1 - 2v)$ represents the bulk modulus of the coal and K_s represents the bulk modulus of the coal grains, Pa; α is the Biot coefficient, and can be expressed as $\alpha = 1 - K/K_s$; E is the Young's Modulus of the coal, Pa; E_s is the Young's Modulus of the coal grains, Pa; v is Poisson's Ratio; δ_{ij} is the Kronecker delta tensor defined as 1 for $i = j$ and 0 for $i \neq j$; f_i denotes the components of the body forces; and $\sigma_{kk} = \sigma_{11} + \sigma_{22} + \sigma_{33}$. A Langmuir-type equation is then used to define the sorption-induced volumetric strain, which can be expressed as [50] $\varepsilon_s = \varepsilon_L p_m / (p_L + p_m)$, in which ε_L is the maximum volumetric strain, and effective stresses are defined as $\sigma_{ij}^e = \sigma_{ij} - \alpha p_f$ [51,52].

Combining Equations (A16)–(A18):

$$Gu_{i,jj} + \frac{G}{1 - 2v}u_{i,ji} - \alpha p_{m,i} - \beta p_{f,i} - K\varepsilon_{s,i} + f_i = 0 \tag{A19}$$

yields a modified Navier-type equation [53] defining deformation.

Appendix A.1.3. Fracture-Matrix Cross-Coupling

The permeability and porosity represent the key cross-coupling parameters linking the hydrological and mechanical fields.

Matchstick conceptual models have been widely used to describe matrix-cleat systems and to derive several permeability models (Figure A1a). The cubic law is widely applied to describe permeability change relative to the porosity field as [11]:

$$\frac{k}{k_0} = \left(\frac{\varphi}{\varphi_0}\right)^3 \tag{A20}$$

where the subscript *0* refers to the initial state; and k, φ are the absolute permeability and porosity, respectively.
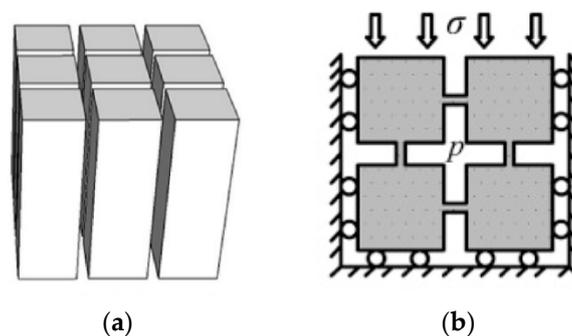

(a)   (b)

Figure A1. Simplified model of the coal and idealized boundary conditions in a CBM reservoir [54], (**a**) matchstick conceptual model, (**b**) uniaxial strain for a coal seam under constant vertical stress conditions.

A variety of analytical permeability models have been developed to predict the unique permeability behaviors of CBM reservoirs, including the Gray, Seidle-Huitt, Harpalani and Chen, Shi-Durucan,

Cui-Bustin, and the Robertson-Christiaansen models [20,55]. Thus, permeability may be linked to the evolution of porosity and strain. The strain field may be defined as (Equation (A19)):

$$\varepsilon_v = -\frac{1}{K}\left(\sigma^- - \alpha p_f\right) + \varepsilon_s \tag{A21}$$

where $\varepsilon_v = \varepsilon_{11} + \varepsilon_{22} + \varepsilon_{33}$ is the volumetric strain of the coal matrix; and $\sigma^- = -\sigma_{kk}/3$ represents the mean compressive stress. Porosity changes with the effective strain as:

$$\varphi_f - \varphi_{f0} = \left(\alpha - \varphi_f\right)\Delta\varepsilon_e \tag{A22}$$

where $\Delta\varepsilon_e = \Delta\varepsilon_v + \Delta p_f/K_s - \Delta\varepsilon_s$ is defined as the effective volumetric strain; $\Delta\varepsilon_v$ represents the total volumetric strain; $\Delta p_f/K_s$ denotes the compaction strain of the coal grains; and $\Delta\varepsilon_s$ represents the gas sorption-induced volumetric strain.

For example, if the initial porosity is φ_{f0} at pressure p_{f0} and the initial volumetric strain ε_{v0} is zero, then the porosity change ratio can be expressed as:

$$\frac{\varphi_f}{\varphi_{f0}} = \frac{1}{1+S}\left[(1 + S_0) + \frac{\alpha}{\varphi_{f0}}(S - S_0)\right] \tag{A23}$$

where $S = \varepsilon_v + \left(p_f/K_s\right) - \varepsilon_s$, $S_0 = \left(p_{f0}/K_s\right) - \varepsilon_L P_{m0}/(P_{m0} + p_L)$.

Under the conditions of uniaxial strain and constant overburden load, $S \ll 1$, $S_0 \ll 1$, $K_s \gg K$, and a simplified expression for the porosity is recovered from Equation (A24) as [56]:

$$\frac{\varphi_f}{\varphi_{f0}} = 1 + \frac{(1+v)(1-2v)}{E(1-v)\varphi_{f0}}\left(p_f - p_{f0}\right) - \frac{2(1-2v)\varepsilon_L}{3(1-v)\varphi_{f0}}\left(\frac{p_m}{p_m + P_L} - \frac{p_{m0}}{p_{m0} + P_L}\right) \tag{A24}$$

where p_{fg} indicates the current reservoir pressure, Pa, which is the same as in the P-M model previously presented by Palmer and Mansoori [57–59].

The Palmer and Mansoori model is one of the most commonly used analytical permeability models (P-M Model), as detailed in Figure A1b. A critical review of the interactions between multiple processes during CBM extraction indicates that permeability models under uniaxial strain are not necessarily applicable to variable stress conditions. However, the P-M Model is chosen as the foundation model for the simulation of absolute permeability in this study, expressed as [60,61]:

$$\frac{k}{k_0} = \left[1 + \frac{1}{M\varphi_{f0}}\left(p_f - p_{f0}\right) - \frac{\varepsilon_L}{\varphi_{f0}}\left(\frac{K}{M} - 1\right)\left(\frac{p_m}{p_m + P_L} - \frac{p_{m0}}{p_{m0} + P_L}\right)\right]^3 \tag{A25}$$

where $M = E(1-v)/(1+v)(1-2v)$ represents the constrained axial modulus.

Water and gas coexist in many CBM reservoirs. Therefore, the effective permeability, as a function of the relative permeability with the absolute permeability representing the most significant parameter for the two-phase flow. The relative permeability models of Equations (A26) and (A27) at saturation S_w are widely used [62]. Calibrating the endpoint relative permeability for gas slippage, a dynamic effective permeability model may be expressed as [63–65]:

$$k_{rg} = \left[1 - \left(\frac{S_w - S_{wr}}{1 - S_{wr} - S_{gr}}\right)\right]^2\left[1 - \left(\frac{S_w - S_{wr}}{1 - S_{wr}}\right)^2\right] \tag{A26}$$

$$k_{rw} = \left(\frac{S_w - S_{wr}}{1 - S_{wr}}\right)^4 \tag{A27}$$

$$k_{eg} = k\left(1 + \frac{b}{p}\right)k_{rg}k_{rg0} \tag{A28}$$

$$k_{ew} = kk_{rg}k_{rw0} \tag{A29}$$

where k_{rg} represents the relative permeability of the gas and is dimensionless (-); k_{rw} is the relative permeability of water (-); k_{rg0} indicates the endpoint relative permeability of the gas (-); k_{rw0} denotes the endpoint relative permeability of water (-); S_{wr} represents the irreducible water saturation fraction (-); S_{gr} is the residual gas saturation fraction (-); and b denotes the slippage factor.

Appendix A.2. Coupled Relationship

The hydraulic and mechanical fields are defined by Equations (A13)–(A15), and (A19) and the cross-coupling term of Equations (A24)–(A27) complete the H-M coupled model, as shown in Figure A2 These equations are implemented into the solid mechanics and PDE modules of COMSOL Multiphysics to solve the reservoir evolution of steeply-dipping UTCBM reservoirs. The solid mechanics module is used to describe Equation (A19) and gas diffusion in the matrix and the two-phase flow in the fracture system are represented by the PDE modules (Equations (A13)–(A15)).
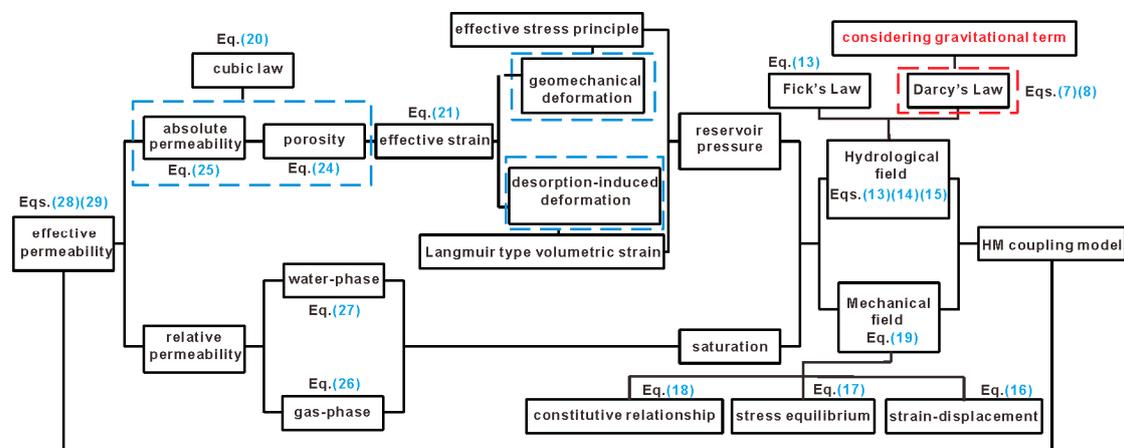

Figure A2. Interactions of multiple processes during CBM extraction.

References

1. Wang, L.; Chen, Z.; Wang, C.; Elsworth, D.; Liu, W. Reassessment of Coal Permeability Evolution Using Steady-state Flow Methods: The Role of Flow Regime Transition. *Int. J. Coal Geol.* **2019**, *211*, 103210. [CrossRef]
2. Lu, M.; Connell, L.D. A model for the flow of gas mixtures in adsorption dominated dual porosity reservoirs incorporating multi-component matrix diffusion: Part I. Theoretical development. *J. Petrol. Sci. Eng.* **2007**, *59*, 17–26. [CrossRef]
3. Aminian, K.; Ameri, S. Predicting production performance of CBM reservoirs. *J. Nat. Gas Sci. Eng.* **2009**, *1*, 25–30. [CrossRef]
4. Du, Y.; Chen, X.; Li, L.; Wang, P. Characteristics of methane desorption and diffusion in coal within a negative pressure environment. *Fuel* **2018**, *217*, 111–121. [CrossRef]
5. Karacan, C.Ö.; Ruiz, F.A.; Cotè, M.; Phipps, S. Coal mine methane: A review of capture and utilization practices with benefits to mining safety and to greenhouse gas reduction. *Int. J. Coal Geol.* **2011**, *86*, 121–156. [CrossRef]
6. Pan, Z.; Wood, D.A. Coalbed methane (CBM) exploration, reservoir characterisation, production, and modelling: A collection of published research (2009–2015). *J. Nat. Gas Sci. Eng.* **2015**, *26*, 1472–1484. [CrossRef]
7. Xia, T.; Zhou, F.; Liu, J.; Hu, S.; Liu, Y. A fully coupled coal deformation and compositional flow model for the control of the pre-mining coal seam gas extraction. *Int. J. Rock Mech. Min. Sci.* **2014**, *72*, 138–148. [CrossRef]
8. Wan, Y.; Liu, Y.; Ouyang, W.P.; Liu, W.; Han, G. Desorption area and pressure-drop region of wells in a homogeneous coalbed. *J. Nat. Gas Sci. Eng.* **2016**, *28*, 1–14. [CrossRef]
9. Li, H.; Lau, H.C.; Huang, S. China's coalbed methane development: A review of the challenges and opportunities in subsurface and surface engineering. *J. Petrol. Sci. Eng.* **2018**, *166*, 621–635. [CrossRef]

10. Kong, X.; Wang, E.; Liu, Q.; Li, D.; Li, Z.; Gao, Z. Dynamic permeability and porosity evolution of coal seam rich in CBM based on the flow-soild coupling theory. *J. Nat. Gas Sci. Eng.* **2017**, *40*, 61–71. [CrossRef]

11. Cui, X.; Bustin, R.M. Volumetric strain associated with methane desorption and its impact on coalbed gas production from deep coal seams. *Int. J. Coal Geol.* **2005**, *89*, 1181–1202. [CrossRef]

12. Li, S.; Tang, D.; Pan, Z.; Xu, H.; Tao, S.; Liu, Y.; Ren, P. Geological conditions of deep coalbed methane in the eastern margin of the Ordos Basin, China: Implications for coalbed methane development. *J. Nat. Gas Sci. Eng.* **2018**, *53*, 394–402. [CrossRef]

13. Wang, S.; Wang, F.; Hou, G.; Wu, X.; Zhang, C.; Zhang, Y.; Hu, Q. CBM development well type for steep seam in Fukang Baiyanghe mining area Xinjiang. *J. China Coal Soc.* **2014**, *39*, 1914–1918.

14. Jiang, R.; Wang, Y.; Li, H.; Yang, M. A numerical simulation on the impact of coal seam dip on productivity of CBM horizontal well. *J. China Coal Soc.* **2015**, *40*, 151–157.

15. Fu, X.; Kang, J.; Liang, S.; Gao, L.; Chen, X. Well type optimization and physical property in gas drainage process of steep inclined coal reservoir in Fukang Western Block. *Coal Sci. Technol.* **2018**, *46*, 9–16.

16. Kang, J.; Fu, X.; Gao, L.; Liang, S. Production profile characteristics of large dip angle coal reservoir and its impact on coalbed methane production: A case study on the Fukang west block, southern Junggar Basin, China. *J. Petrol. Sci. Eng.* **2018**, *171*, 99–114. [CrossRef]

17. Wang, C.; Peng, X.; Zhu, S.; Sun, H.; Zhang, J.; Lin, L. Coalbed methane well-type optimization and well pattern arrangement for thick coal seam with a large dip angle. *Chin. J. Rock Mech. Eng.* **2019**, *38*, 1–8.

18. Reid, G.W.; Towler, B.F.; Harris, H.G. Simulation and economics of coalbed methane production in the powder river basin. In Proceedings of the SPE Rocky Mountain Regional Meeting, Casper, WY, USA, 18–21 May 1992.

19. Sparks, D.P.; McLendon, T.H.; Saulsberry, J.L.; Lambert, S.W. The effects of stress on coalbed reservoir performance, Black Warrior Basin, U.S.A. In Proceedings of the SPE Annual Technical Conference and Exhibition, Dallas, TX, USA, 2–25 October 1995; Society of Petroleum Engineers, Inc.: Dallas, TA, USA, 1995.

20. Pan, Z.; Connell, L.D. Modelling permeability for coal reservoirs: A review of analytical models and testing data. *Int. J. Coal Geol.* **2012**, *92*, 1–44. [CrossRef]

21. Shi, J.; Durucan, S. Modelling laboratory horizontal stress and coal permeability data using S&D permeability model. *Int. J. Coal Geol.* **2014**, *131*, 172–176.

22. Connell, L.D.; Lu, M.; Pan, Z.J. An analytical coal permeability model for tri-axial strain and stress conditions. *Int. J. Coal Geol.* **2010**, *84*, 103–114. [CrossRef]

23. Chen, Y.; Liu, D.; Yao, Y.; Chen, L. Dynamic permeability change during coalbed methane production and its controlling factors. *J. Nat. Gas Sci. Eng.* **2015**, *25*, 335–346. [CrossRef]

24. Connell, L.D. A new interpretation of the response of coal permeability to changes in pore pressure, stress and matrix shrinkage. *Int. J. Coal Geol.* **2016**, *162*, 169–182. [CrossRef]

25. Zhang, S.; Liu, J.; Wei, M.; Elsworth, D. Coal permeability maps under the influence of multiple coupled process. *Int. J. Coal Geol.* **2018**, *187*, 71–82. [CrossRef]

26. Shen, J.; Qin, Y.; Wang, G.; Fu, X.; Wei, C.; Lei, B. Relative permeabilities of gas and water for different rank coals. *Int. J. Coal Geol.* **2011**, *86*, 266–275. [CrossRef]

27. Bertrand, F.; Cerfontaine, B.; Collin, F. A fully coupled hydro-mechanical model for the modeling of coalbed methane recovery. *J. Nat. Gas Sci. Eng.* **2017**, *46*, 307–325. [CrossRef]

28. Clarkson, C.R.; Jordan, C.L.; Gierhart, R.R.; Seidle, J.P. Production data analysis of coalbed-methane wells. *SPE Reserv. Eval. Eng.* **2008**, *11*, 311–325. [CrossRef]

29. Minkoff, S.E.; Stone, C.M.; Bryant, S.; Peszynska, M.; Wheeler, M.F. Coupled fluid flow and geomechanical deformation modeling. *J. Petrol. Sci. Eng.* **2003**, *38*, 37–56. [CrossRef]

30. Wu, Y.; Liu, J.; Elsworth, D.; Miao, X.; Mao, X. Development of anisotropic permeability during coalbed methane production. *J. Nat. Gas Sci. Eng.* **2010**, *2*, 197–210. [CrossRef]

31. Zhu, W.; Wei, C.; Liu, J.; Qu, H.; Elsworth, D. A model of coal-gas interaction under variable temperatures. *Int. J. Coal Geol.* **2011**, *86*, 213–221. [CrossRef]

32. Fan, C.; Li, S.; Luo, M.; Yang, Z.; Zhang, H.; Wang, S. Deep CBM extraction numerical simulation based on hydraulic-mechanical-thermal coupled model. *J. China Coal Soc.* **2016**, *41*, 3076–3085.

33. Li, S.; Fan, C.; Han, J.; Luo, M.; Yang, Z.; Bi, H. A fully coupled thermal-hydraulic-mechanical model with two-phase flow for coalbed methane extraction. *J. Nat. Gas Sci. Eng.* **2016**, *33*, 324–336. [CrossRef]

34. Fan, C.; Elsworth, D.; Li, S.; Zhou, L.; Yang, Z.; Song, Y. Thermo-hydro-mechanical-chemical couplings controlling CH_4 production and CO_2 sequestration in enhanced coalbed methane recovery. *Energy* **2019**, *173*, 1054–1077. [CrossRef]

35. Dong, J.; Chen, Y.; Jin, K.; Zhang, H.; Liu, Q.; Jiang, J.; Hu, B. Effects of diffusion and suction negative pressure on coalbed methane extraction and a new measure to increase the methane utilization rate. *Fuel* **2017**, *197*, 70–81. [CrossRef]

36. Liu, J.; Chen, Z.; Elsworth, D.; Qu, H.; Chen, D. Interactions of multiple processes during CBM extraction: A critical review. *Int. J. Coal Geol.* **2011**, *87*, 175–189. [CrossRef]

37. Zhang, J.; Feng, Q.; Zhang, X.; Wen, S.; Zhai, Y. Relative Permeability of Coal: A Review. *Transp. Porous Med.* **2015**, *106*, 63–594. [CrossRef]

38. Müller, N. Supercritical CO_2-brine relative permeability experiments in reservoir rocks-literature review and recommendations. *Transp. Porous Med.* **2011**, *87*, 367–383. [CrossRef]

39. Kang, J.; Fu, X.; Liang, S.; Li, X.; Chen, X.; Wang, Z. A numerical simulation study on the characteristics of the gas production profile and its formation mechanisms for different dip angles in coal reservoirs. *J. Petrol. Sci. Eng.* **2019**, *181*, 106198. [CrossRef]

40. Tao, S.; Pan, Z.; Tang, S.; Chen, S. Current status and geological conditions for the applicability of CBM drilling technologies in China: A review. *Int. J. Coal Geol.* **2019**, *202*, 95–108. [CrossRef]

41. Wang, L.; Vandamme, M.; Pereira, J.M.; Dangla, P.; Espinoz, N. Permeability changes in coal seams: The role of anisotropy. *Int. J. Coal Geol.* **2018**, *199*, 52–64. [CrossRef]

42. Wang, Z.; Pan, J.; Hou, Q.; Niu, Q.; Tian, J.; Wang, H.; Fu, X. Changes in the anisotropic permeability of low-rank coal under varying effective stress in Fukang mining area, China. *Fuel* **2018**, *234*, 1484–1497. [CrossRef]

43. Koenig, R.A.; Stubbs, P.B. Interference testing of a coalbed methane reservoir. In *SPE Unconventional Gas Technology Symposium*; Society of Petroleum Engineers, Inc.: Louisville, KY, USA, 1986.

44. Yan, Z.; Wang, K.; Zang, J.; Wang, C.; Liu, A. Anisotropic coal permeability and its stress sensitivity. *Int. J. Min. Sci. Technol.* **2019**, *29*, 507–511. [CrossRef]

45. Zhao, Y.; Lin, B.; Liu, T.; Li, Q.; Kong, J. Gas flow field evolution around hydraulic slotted borehole in anisotropic coal. *J. Nat. Gas Sci. Eng.* **2018**, *58*, 189–200. [CrossRef]

46. Liu, Q.; Cheng, Y.; Wang, H.; Zhou, H.; Wang, L.; Li, W.; Liu, H. Numerical assessment of the effect of equilibration time on coal permeability evolution characteristics. *Fuel* **2015**, *140*, 81–89. [CrossRef]

47. An, F.; Cheng, Y.; Wang, L.; Li, W. A numerical model for outburst including the effect of adsorbed gas on coal deformation and mechanical properties. *Comput. Geotech.* **2013**, *54*, 222–231. [CrossRef]

48. Ziarani, A.S.; Aguilera, R.; Clarkson, C.R. Investigating the effect of sorption time on coalbed methane recovery through numerical simulation. *Fuel* **2011**, *90*, 2428–2444. [CrossRef]

49. Liu, J.; Chen, Z.; Elsworth, D.; Miao, X.; Mao, X. Evolution of coal permeability from stress-controlled to displacement-controlled swelling conditions. *Fuel* **2011**, *90*, 2987–2997. [CrossRef]

50. Liu, J.; Chen, Z.; Elsworth, D.; Miao, X.; Mao, X. Evaluation of stress-controlled coal swelling processes. *Int. J. Coal Geol.* **2010**, *83*, 446–455. [CrossRef]

51. Gao, F.; Xue, Y.; Gao, Y.; Zhang, Z.; Teng, T.; Liang, X. Fully coupled thermo-hydro-mechancil model for extraction of coal seam gas with slotted boreholes. *J. Nat. Gas Sci. Eng.* **2016**, *31*, 226–235. [CrossRef]

52. Chen, M.; Chen, Z. Effective stress laws for multi-porosity media. *Appl. Math. Mech.* **1999**, *20*, 1207–1213.

53. Wu, Y.; Liu, J.; Elsworth, D.; Siriwardane, H.; Miao, X. Evolution of coal permeability: Contribution of heterogeneous swelling processes. *Int. J. Coal Geol.* **2011**, *88*, 152–162. [CrossRef]

54. Lu, S.; Cheng, Y.; Li, W. Model development and analysis of the evolution of coal permeability under different boundary conditions. *J. Nat. Gas Sci. Eng.* **2016**, *31*, 129–138. [CrossRef]

55. Gray, I. Reservoir engineering in coal seams: Part 1-the physical process of gas storage and movement in coal seams. *SPE Reserv. Eng.* **1987**, *2*, 28–34. [CrossRef]

56. Zhang, H.; Liu, J.; Elsworth, D. How sorption-induced matrix deformation affects gas flow in coal seams: A new FE model. *Int. J. Rock Mech. Min. Sci.* **2008**, *45*, 1226–1236. [CrossRef]

57. Palmer, I.; Mansoori, J. How permeability depends on stress and pore pressure in coalbeds: A new model. In Proceedings of the SPE Annual Technical Conference and Exhibition, Denver, CO, USA, 6–9 October 1996.

58. Palmer, I.; Mansoori, J. How permeability dependence on stress and pore pressure in coalbeds: A new model. *SPEREE* **1998**, *1*, 539–544. [CrossRef]

59. Palmer, I. Permeability changes in coal: Analytical modeling. *Int. J. Coal Geol.* **2009**, *77*, 119–126. [CrossRef]

60. Sun, Z.; Shi, J.; Zhang, T.; Wu, K.; Feng, D.; Sun, F.; Huang, L.; Hou, C.; Li, X. A fully-coupled semi-analytical model for effective gas/water phase permeability during coal-bed methane production. *Fuel* **2018**, *23*, 44–52. [CrossRef]

61. Zhao, J.; Tang, D.; Xu, H.; Meng, Y.; Lv, Y.; Tao, S. A dynamic prediction model for gas-water effective permeability in unsaturated coalbed methane reservoirs based on production data. *J. Nat. Gas Sci. Eng.* **2014**, *21*, 496–509. [CrossRef]

62. Corey, A.T. The interrelation between gas and oil relative permeability. *Prod. Mon.* **1954**, *31*, 533–546.

63. Chen, D.; Pan, Z.; Liu, J.; Connell, L.D. An improved relative permeability model for coal reservoirs. *Int. J. Coal Geol.* **2013**, *109–110*, 45–57. [CrossRef]

64. Xu, H.; Tang, D.; Tang, S.; Zhao, J.; Meng, Y. A dynamic prediction model for gas-water effective permeability based on coalbed methane production data. *Int. J. Coal Geol.* **2013**, *121*, 44–52. [CrossRef]

65. Li, B.; Yang, K.; Xu, P.; Xu, J.; Yuan, M.; Zhang, M. An experimental study on permeability characteristics of coal with slippage and temperature effects. *J. Petrol. Sci. Eng.* **2019**, *175*, 294–302. [CrossRef]